



# Flexural behavior of high strength concrete filled high strength square steel tube



Guochang Li<sup>a</sup>, Di Liu<sup>a</sup>, Zhijian Yang<sup>a,\*</sup>, Chunyu Zhang<sup>b</sup>

<sup>a</sup> School of Civil Engineering, Shenyang Jianzhu University, Shenyang 110168, China

<sup>b</sup> Department of Civil and Environmental Engineering and Construction, University of Nevada Las Vegas, 89119, USA

## ARTICLE INFO

### Article history:

Received 27 May 2016

Received in revised form 5 October 2016

Accepted 12 October 2016

Available online xxxx

### Keywords:

High strength square steel tube

High strength concrete

Experimental study

Pure bending

Finite element analysis (FEA)

## ABSTRACT

To study the mechanical behavior of high-strength concrete filled high-strength square steel tube (HCFHST) under pure bending load, six specimens with different steel ratio were tested. The corresponding nonlinear finite-element models were established to analyze the mechanical properties. The load-displacement curves obtained from the numerical analyses are consistent with the experimental results. In addition, the influences of different materials are analyzed in this paper. The moment-curvature relationship can be divided into three stages: elastic stage, yield stage and hardening stage. And the ultimate bearing capacity increased with the steel ratio, steel yield strength and concrete compressive strength. Moreover, the ultimate bearing capacity of the experiment and finite-element analysis (FEA) model is compared with the requirements of codes: AISC-LRFD (1999), AIJ (1997), EC4 (1994) and GB50936-2014 (2014). The test and FEA result were the most compatible to the calculated result of EC4 (1994). And find the results in this paper is the most compatible to the code EC4 (1994).

© 2016 Elsevier Ltd. All rights reserved.

## 1. Introduction

Compared with traditional reinforced concrete structure, concrete filled steel tube (CFST) has a higher bearing capacity, ductility and fire resistant capacity. Besides, it's also an economic structure type and can be constructed easily. Because of these characteristics, it has been widely used in practical engineering such as high-rise buildings and long-span bridges. The modern building has a higher demand for the construction height and span length. Therefore, the structure design becomes more ponderous. High-strength concrete filled high-strength square steel tube (HCFHST), which takes the advantage of both high-strength concrete and high-strength square steel tube can raise the ultimate bearing capacity and decrease the weight of the structure.

Varma et al. [1,2] presented an experiment of monotonic and cyclic load on CFST column. The results showed that ACI code can predict bearing capacity of high strength CFST beam-column accurately. Liu et al. [3] conducted an experiment on 22 high strength rectangular CFST columns, which showed that ultimate bearing capacity decreased with the rise of depth-width ratio. Liu et al. [4] reported the test results of 12 high strength rectangular CFST beams, the result illustrated that the formula of EC4, ACI and AIJ codes to calculate bearing capacity for high strength CFST need to be modified. Liu et al. [5] designed an experiment on 26 CFST specimens under axial compression load, the results

showed that the code EC4 overestimated the ultimate bearing capacity of the specimens. Young et al. [6] presented an experimental investigation of concrete filled cold-formed high-strength stainless steel tube columns, and proposed design recommendations for design. Mursi et al. [7,8] reported the test and analysis results of high strength steel columns subjected to bi-axial bending. Choi et al. [9] proposed a simplified strength formula to establish the P–M interaction curve of CFST with concrete strength up to 100 MPa. The results indicated that the simplified formula could greatly improve the accuracy of the results and reduce the effort of calculation. Chung et al. [10] compared some existing material models of the steel and concrete, and proposed a non-linear fiber element method. Jung et al. [11] did a test study on 4 high strength CFST columns. The results showed that ultimate strength of steel and concrete can influence the axial bearing capacity and ductility of specimens. Chung et al. [13] investigated 6 HCFHST beam specimens. The calculated results of numerical method were consistent with the test results. Guler et al. [14] studied the influence of steel tube thickness and bond strength on bearing capacity and ductility of square and circular high strength CFST columns. Li et al. [15] studied the mechanical behavior of HCFHST column under axial load by finite-element analysis (FEA), the results shows that the FEA result of bearing capacity are consistent with different codes. Patel et al. [16] presented a new efficient numerical model to predict the cyclic performance of high strength rectangular CFST slender beam-columns. Kim et al. [17] presented an experiment on 2 CFST columns and 4 concrete encased steel columns with high strength steel and high strength concrete.

\* Corresponding author.

E-mail address: faemail@163.com (Z. Yang).

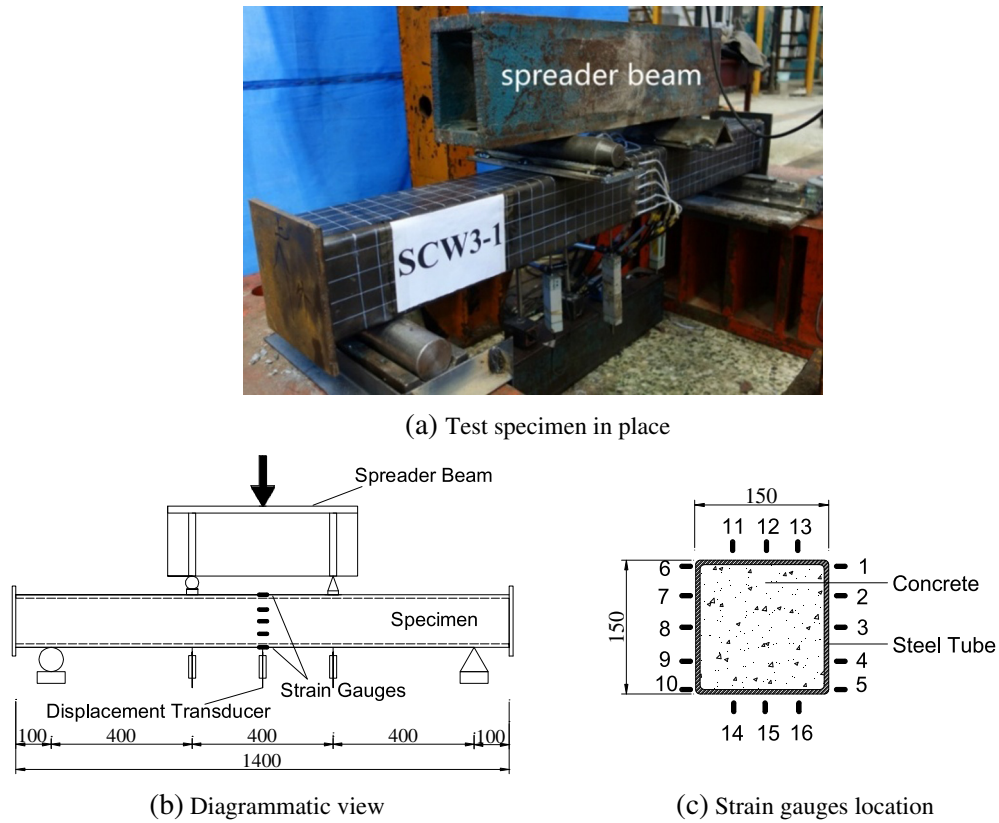


Fig. 1. Test setup.

Table 1  
Details of the specimens.

No.	Specimens	$B \times t \times L_0$ (mm $\times$ mm $\times$ mm)	$\alpha$	$\xi$	$f_y$ (MPa)	$f_u$ (MPa)	$f_{cu}$ (MPa)
1	SCW1-1	150 $\times$ 4 $\times$ 1200	0.116	0.699	434.56	546.2	98
2	SCW1-2	150 $\times$ 4 $\times$ 1200	0.116	0.692	430.00	547	98
3	SCW2-1	150 $\times$ 5 $\times$ 1200	0.148	0.863	420.00	516	98
4	SCW2-2	150 $\times$ 5 $\times$ 1200	0.148	0.855	416.30	513.7	98
5	SCW3-1	150 $\times$ 6 $\times$ 1200	0.181	1.084	430.00	545	98
6	SCW3-2	150 $\times$ 6 $\times$ 1200	0.181	1.101	436.90	550.4	98

Note:  $B$  is the width of the steel tube,  $t$  is the tube wall thickness,  $L_0$  is the calculated length.  $\alpha$  is the steel ratio ( $\alpha = A_s / A_c$ , where  $A_s, A_c$  are the cross-section area of steel tube and concrete),  $\xi$  is the confinement factor ( $\xi = A_s f_y / A_c f_{ck}$ ),  $f_y$  is steel yield strength,  $f_u$  is the steel ultimate strength and  $f_{cu}$  is the 28-day concrete cube strength.

CFST member has no advantages to bear bending load alone, therefore it is not suited to be flexural member. In practice project, CFST columns generally subjected to axial and bending load. Pure bending is the

special case of beam-column without axial load, but the flexural behavior of CFST is not independent of the behavior under axial load and axial load–moment interaction. As a result, it is necessary to study the flexural behavior of HCFHST, which is beneficial to know the behavior of HCFHST under eccentric load. Most of the former researches focus on analyzing the HCFHST under the axial loading. However, there are few studies about the HCFHST member under the bending moment. This paper presents a test result of 6 HCFHST beams under pure bending. Besides, the corresponding FEA models were established to predict and compare with the analysis results.

## 2. Experimental investigation

### 2.1. Test design

The test specimens were full-scale models of prototype HCFHST beams under two symmetric load, as shown in Fig. 1(b). Six specimens are in

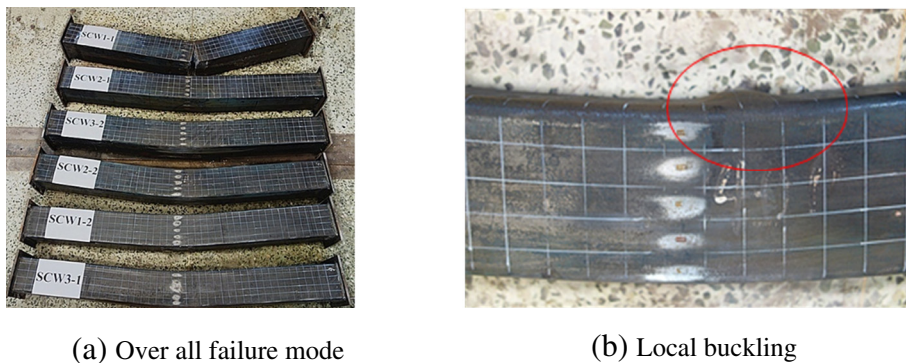


Fig. 2. Failure mode of specimens.

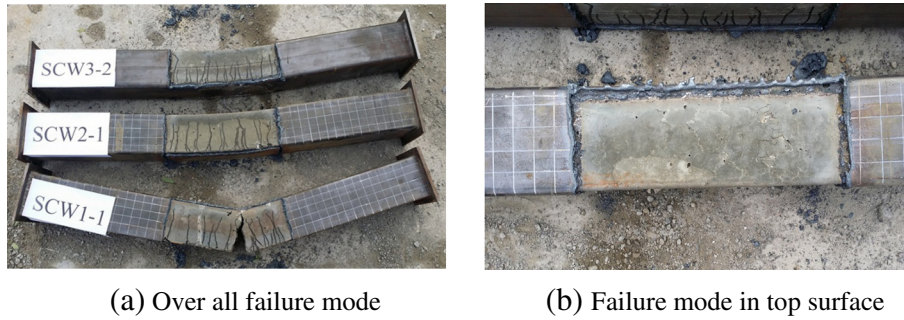


Fig. 3. Failure mode of concrete.

three groups, SCW1-3, with different thickness of the square steel tube, 4 mm, 5 mm, 6 mm, as shown in Table 1. To ensure the reliability, two specimens were tested in each group. The total specimen length and the

clear length are identical for all specimens, as 1400 mm and 1200 mm. For all the specimens, two steel plate with size 200 × 200 × 10 mm were welded at both ends.

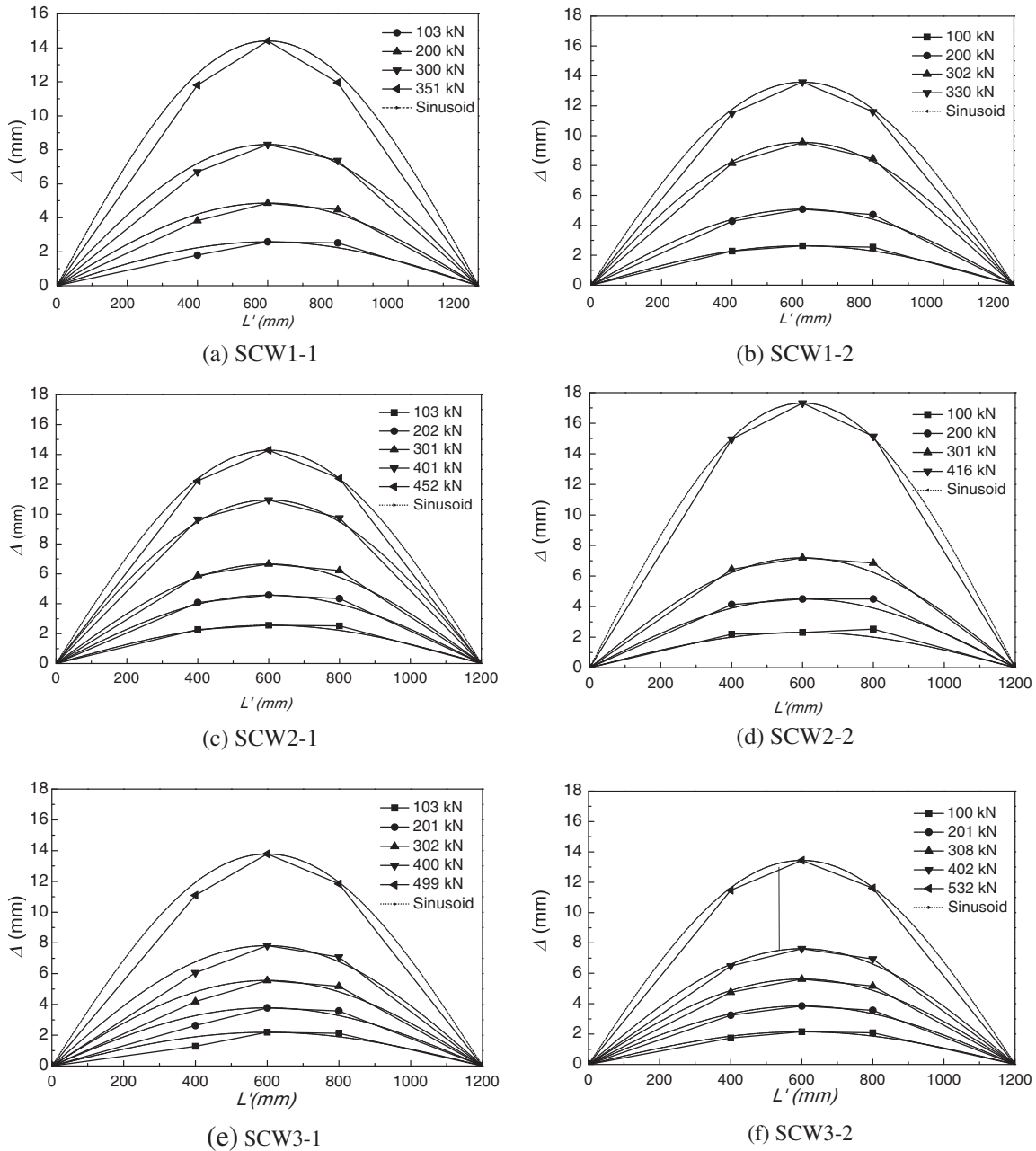


Fig. 4. Distribution of the deflection curves.

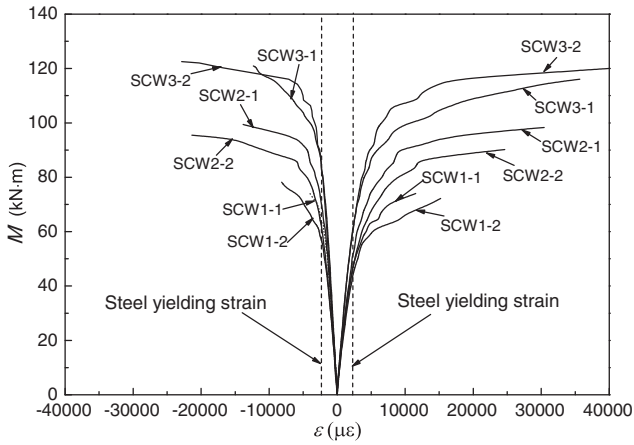
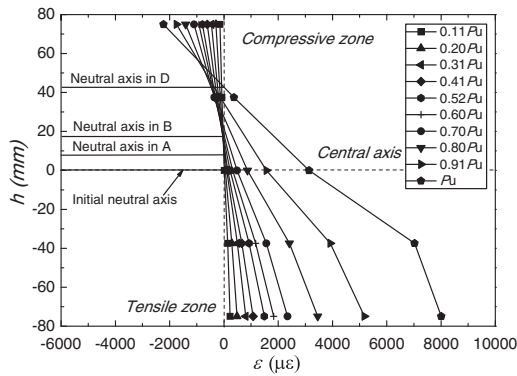


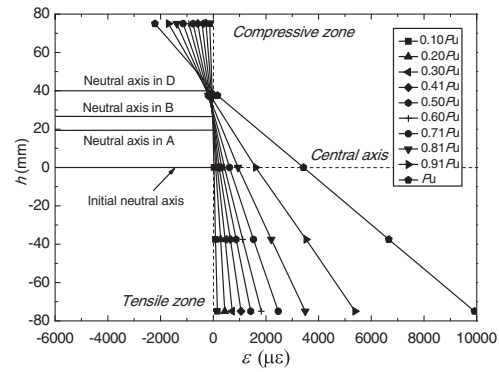
Fig. 5. Bending moment-top (bottom) strain.

As shown in Fig. 1(a) and (b), specimen was simply supported by two metal block on a load frame. The vertical load was applied by a 1000 kN hydraulic jack with load cell, and collected by an automatic system IMP. To measure the longitudinal strain at the mid-span of the specimen, sixteen strain gauges were pasted on the out-surface of the steel tube, as shown in Fig. 1(c). Three displacement transducers were placed to measure the vertical displacement, as shown in Fig. 1(b).

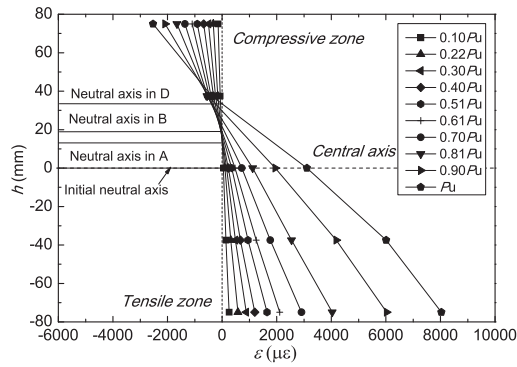
The pure bending condition at the mid-span of the specimen was satisfied by applying two vertical concentrated load, as shown in Fig. 1. The vertical load was applied with a staged increase, which was about 10% of theoretical bending moment capacity of the specimen. At each load level, the vertical load lasted for 2 min. After the specimen yielded, the vertical load was decreased until 1/15 of the theoretical bending moment capacity. The maximum deflection at the mid-span of the specimen was 40 mm.



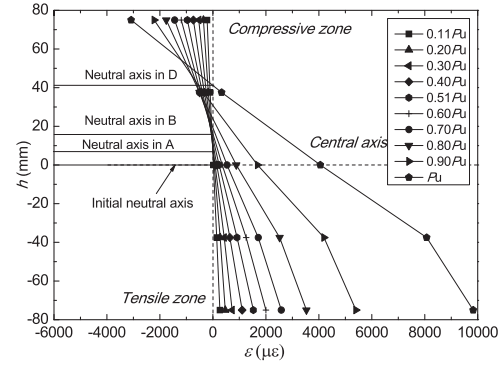
(a) SCW1-1



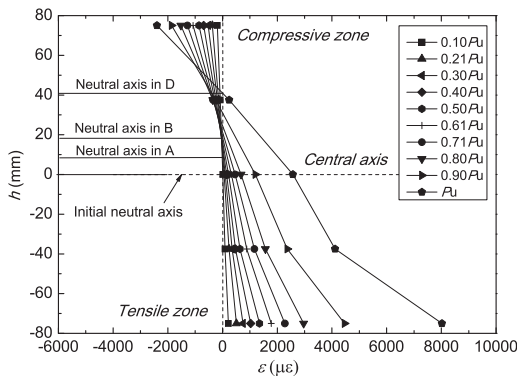
(b) SCW1-2



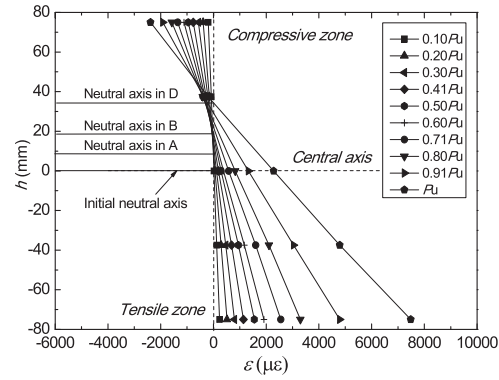
(c) SCW2-1



(d) SCW2-2



(e) SCW3-1



(f) SCW3-2

Fig. 6. Longitudinal strain distribution at mid-span.

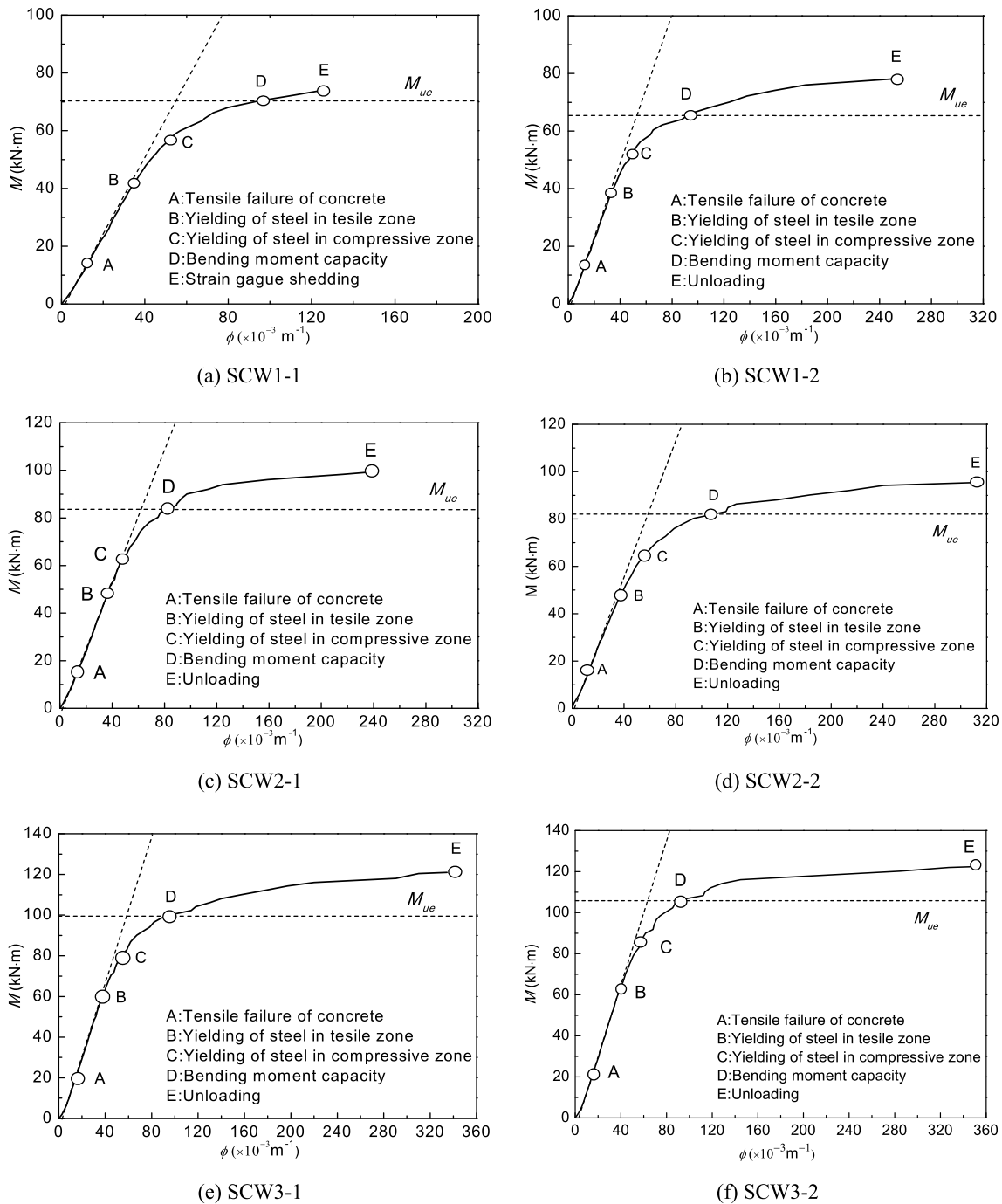


Fig. 7. Curves of bending moment-curvature.

## 2.2. Test results and discussions

### 2.2.1. Failure mode

Tests stopped when the deflection at mid-span got close to the maximum range of the displacement transducer 50 mm. After the deflection at mid-span reached 40 mm (1/30 LO), the bending capacity of the specimen kept increasing. It indicates that the specimen had a high ductility. Failure modes of specimens are shown in Fig. 2. Local buckling appeared at the top surface of the steel tube at mid-span, as shown in Fig. 2 (b). Specimen SCW1-1 breaks because of the continuous loading after large deflection.

To analyze the failure mode of concrete, the mid-span steel tubes were removed after the specimens failed, as shown in Fig. 3. According

to the observation, concrete cracks appeared at the bottom of the beam and extended to about 3/4 of the beam height. The width of the crack were about 1–5 mm.

The concrete in compressive zone did not reach the ultimate compressive strain. The crushing of the concrete were prevented by the steel tube, the specimens exhibited a good ductility performance.

### 2.2.2. Distribution of the deflection curves

The deflection curves of the specimens are shown in Fig. 4. The horizontal and vertical axes indicate the distance to the left support and the vertical deflection. All the deflection curves in Fig. 4 are consistent with the sinusoid curve denoted by the dashed curve.

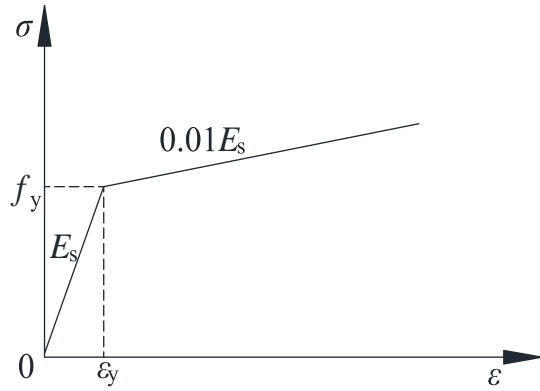


Fig. 8. Stress–strain relation of steel.

### 2.2.3. Bending moment–strain

The bending moment–top (bottom) strain curves are shown in Fig. 5. The results demonstrate that the stiffness of the specimen remains positive after it yields. The ultimate bending moment ( $M_{ue}$ ) is defined as the strength when the tension strain of steel tube at mid-span reaches  $10000 \mu\epsilon$  [18]. Besides, the moment–strain curves of specimens with the same thickness of the steel tube had the similar trend. The ultimate bending moment increases by the thickness of the steel tube. Furthermore, the tensile strain increased faster than the compressive strain after the steel tube yield.

### 2.2.4. Longitudinal strain distribution

To analyze the load distribution in different loading stage, the longitudinal strain of steel tube along the different height at mid-span are measured by the strain gauges and summarized in Fig. 6. It can be seen from Fig. 6 that the cross-section remains almost plane during different loading stage, so it meets the plane cross-section assumption. On the initial loading stage, material remained elastic, and the neutral axis located at the center of the section until the concrete cracked; the neutral axis raised  $0.05\text{--}0.13 h$  toward the compressive side, and kept increasing to  $0.14\text{--}0.2 h$  when tensile steel started to yield; when load reached event D, neutral axis had raised  $0.25\text{--}0.28 h$  toward to the compressive side. The rising speed decreased after concrete quit working in the tensile zone.

### 2.2.5. Bending moment–curvature curves

Fig. 7 indicates the bending moment–curvature curves of different specimens. The curves can be separated into 5 stages by 5 characteristic points (A–E). At point A ( $M_A = 0.2M_{ue}$ ), a short platform appears

between two parallel segments, which indicates that concrete cracked at the tensile side of the specimen. At point B ( $M_B = 0.6M_{ue}$ ), specimen stiffness starts to decrease. At point C ( $M_C = 0.8M_{ue}$ ), steel tube started to yield at the compressive side according to the observation recorder. After point D ( $M_D = M_{ue}$ ), the bearing capacity is still rising, then unloading until bending moment reached the event E.

According to the description of the loading stage of Fig. 7 and the discussion about Fig. 6, the bending moment–curvature relationship at the mid-span of the specimen can be separated into 3 stages: elastic stage, yield stage and hardening stage

#### (1) Elastic stage (OB)

In elastic stage, the stiffness of the specimen remains constant, even if the bottom concrete cracks at point A. In this stage, the deformation of compressive concrete and steel tube keep elastic. Therefore, the whole section remains plane as shown in Fig. 7. And the neutral axis of the specimen increases by the deformation of the bottom steel plate. The elastic stage stops when the bending moment at the mid-span reaches about  $0.2M_{ue}$ , and after that the tensile steel plate starts to yield.

#### (2) Yield stage (BD)

With the increase of the load, the maximum stress of the steel tube in compressive zone exceeded proportional limit as bending moment at  $M_B = 0.6M_{ue}$ ; The longitudinal stress of concrete increased, and the constraining stress produced. Steel tube in tensile zone exceeded proportional limit substantially until bottom surface of steel tube yielded. In this stage, neutral axis ascended, and the growth of curvature was obvious, but moment increased slower than the curvature.

#### (3) Hardening stage (DE)

In hardening stage, the stiffness of the specimen decreases dramatically after point D, but remains positive till the test stopped. In this stage, the axial deformation along the height of the mid-span section can remain almost linear, like specimens SCW 1-2, 2-1 and 3-2, which means that steel tube and concrete work well together. The moment increases slowly, while the curvature raises fast.

## 3. Finite element analysis

### 3.1. Material constitutive model

#### 3.1.1. Steel

To analyze the stress distribution and the interaction between concrete and steel tube, the corresponding FEA models were established

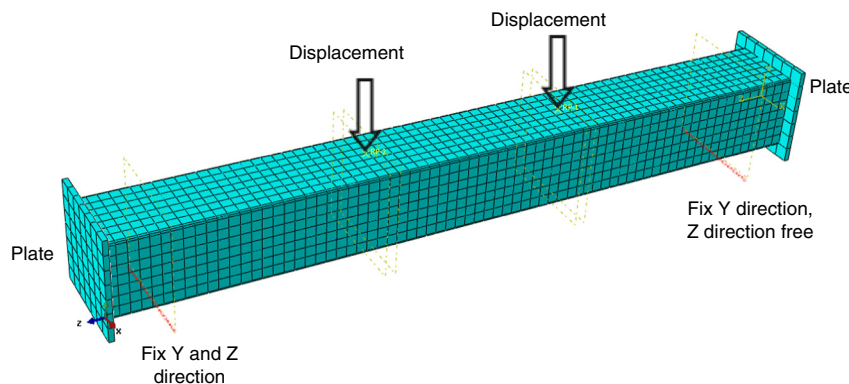


Fig. 9. Simulation boundary conditions.

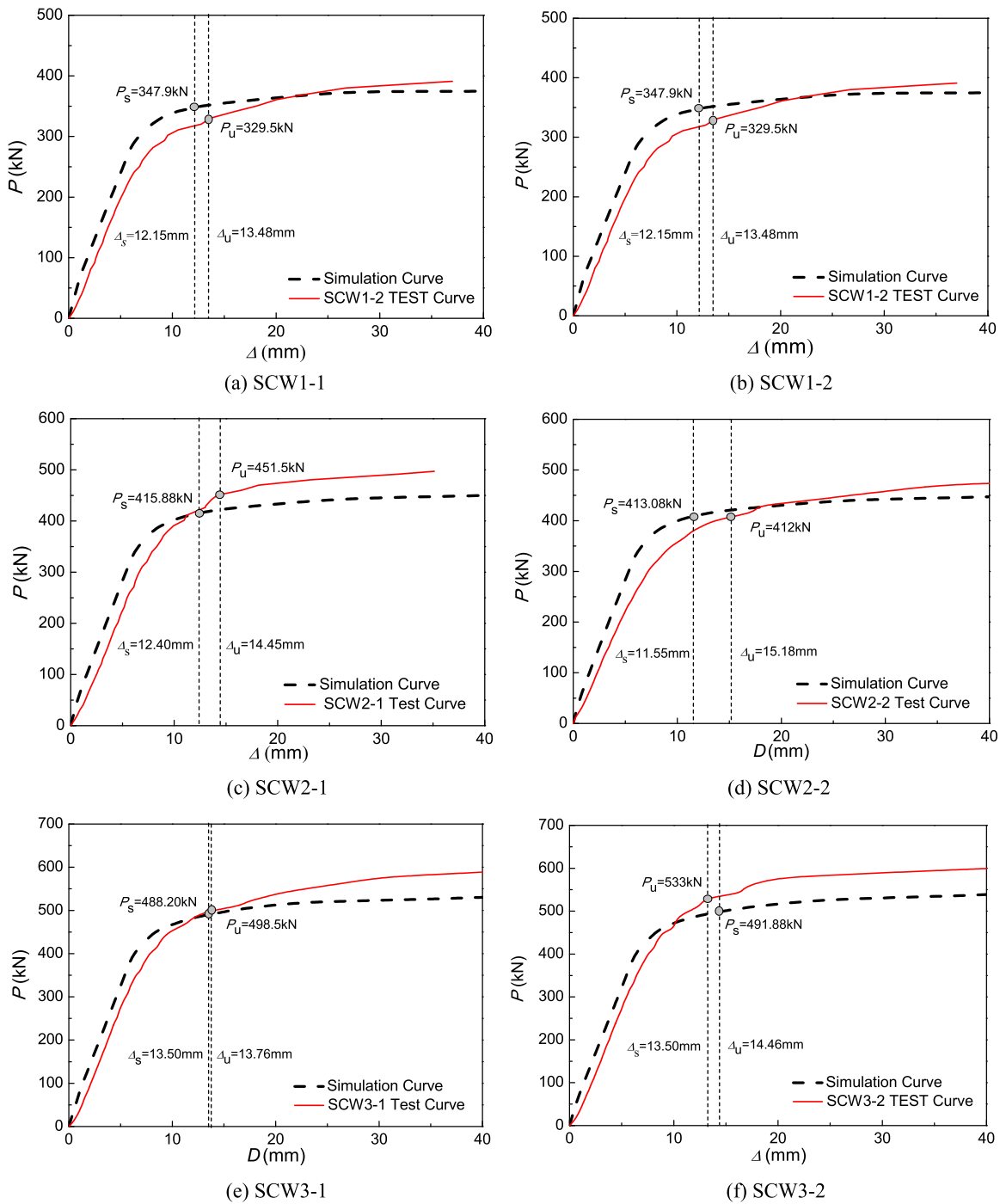


Fig. 10. Comparison of load-deflection between simulation and test results.

**Table 2**  
Comparison of the ultimate bearing capacity and deflection.

Specimen	Simulation value		TEST value		$P_s/P_u$	$\Delta_s/\Delta_u$
	$P_s$ (kN)	$\Delta_s$ (mm)	$P_u$ (kN)	$\Delta_u$ (mm)		
SCW1-1	350.98	12.27	350.5	14.25	1	0.86
SCW1-2	347.90	12.15	329.5	13.48	1.06	0.90
SCW2-1	415.88	12.40	451.5	14.45	0.92	0.86
SCW2-2	413.08	11.55	412.0	15.18	1	0.76
SCW3-1	488.20	13.50	498.5	13.76	0.98	0.98
SCW3-2	491.88	13.50	533.0	14.46	0.92	0.93

Note:  $P_s$ ,  $P_u$  are the bearing capacity of simulation and test data.  $\Delta_s$ ,  $\Delta_u$  are the deflection of simulation and test data.

by ABAQUS/Standard software. The bilinear constitutive model of steel proposed by Han [19] was proved to be suitable for simulating the high-strength steel, as shown in Fig. 8.

This constitutive model was used to simulate the steel tube, as follows:

$$\sigma = \begin{cases} E_s \varepsilon & (\sigma \leq f_y) \\ \sigma_y + (\varepsilon - \varepsilon_y) 0.01 E_s & (\sigma > f_y) \end{cases} \quad (1)$$

where  $\sigma$  is stress,  $\varepsilon$  is strain,  $f_y$  is yield strength,  $\varepsilon_y$  is yield strain,  $E_s$  is elastic modulus, respectively. The elastic modulus  $E_s$  and Poisson's

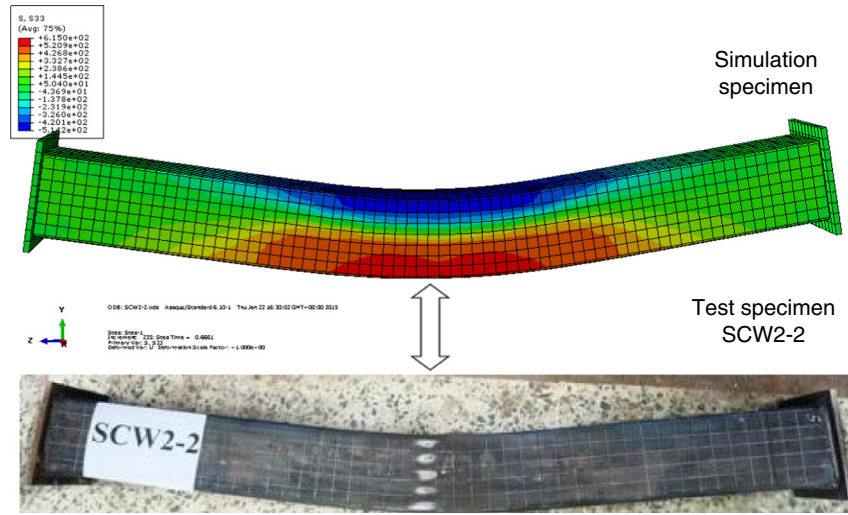


Fig. 11. Comparison of the failure mode.

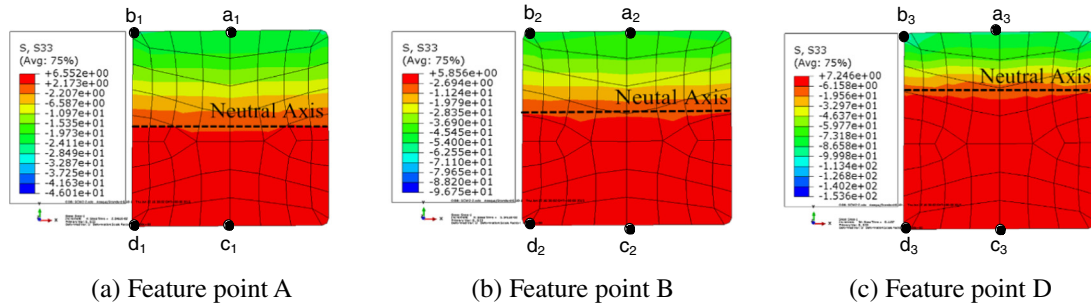


Fig. 12. Concrete stress distribution at mid-span.

ration  $v_s$  were assumed as  $2.06 \times 10^5$  (MPa) and 0.3, the hardening modulus was taken as  $0.01E_s$ .

3.1.2. Concrete

The concrete constitutive model used is the concrete-damaged plasticity model in ABAQUS. The uniaxial compressive stress–strain relation

proposed by Han et al. [20] was used to simulate concrete. The equations for this relation are as follows:

$$y = \begin{cases} 2x - x^2 & (x \leq 1) \\ \frac{x}{\beta_0(x-1)^\eta + x} & (x > 1) \end{cases} \quad (2)$$

where  $x = \varepsilon/\varepsilon_0$ ,  $y = \sigma/\sigma_0$ ,  $\eta = 1.6 + 1.5/x$ ,  $\sigma_0 = f'_c$  (MPa);  $\xi = f_y A_s / f_{ck} A_c \varepsilon_0 = \varepsilon_c + 800\xi^{0.2} \times 10^{-6}$ ,  $\varepsilon_{cc} = 1300 + 12.5f_c \times 10^{-6}$ ,  $\beta_0 = (f'_c)^{0.1} / (1.2\sqrt{1 + \xi})$ ,  $\eta = 1.6 + 1.5/x$ .

In the above equations,  $f_y$  and  $f'_c$  are the yield strength of steel and the cylinder strength of concrete, respectively;  $A_c$  and  $A_s$  are the cross-sectional area of concrete and steel, respectively;  $f_{ck}$  is the characteristic concrete strength.

Table 3

The stress distribution of different stage.

Concrete			Steel tube			
A (MPa)	B (MPa)	D (MPa)	A (MPa)	B (MPa)	D (MPa)	
$a_1$	-23.08	$a_2$ -46.23	$a_3$ -88.96	$a_4$ 140.62	$a_5$ 308.88	$a_6$ 422.09
$b_1$	-24.79	$b_2$ -49.73	$b_3$ -109.08	$b_4$ 144.20	$b_5$ 315.36	$b_6$ 421.25
$c_1$	5.95	$c_2$ 5.36	$c_3$ 4.70	$c_4$ 174.10	$c_5$ 416.59	$c_6$ 434.41
$d_2$	6.03	$d_2$ 5.64	$d_3$ 7.25	$d_4$ 178.27	$d_5$ 416.59	$d_6$ 432.07

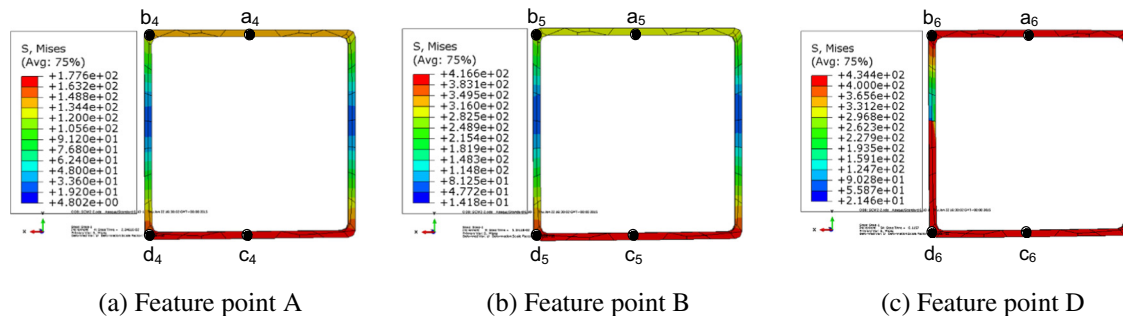


Fig. 13. Steel tube stress distribution.

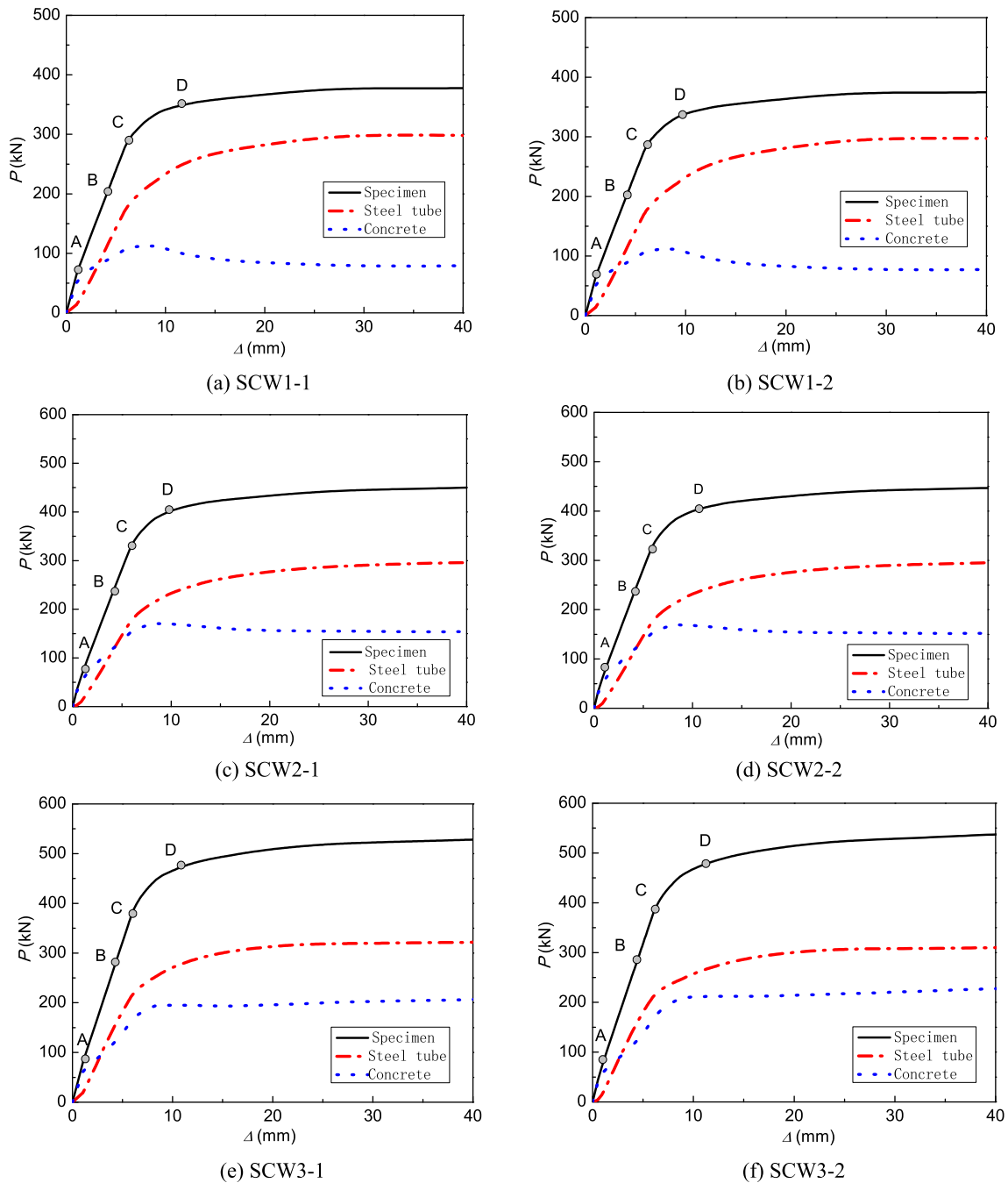


Fig. 14. The load-deflection curve of each components.

**Table 4**  
The percentage of bearing capacity of each part (%).

Specimen	A		B		C		C	
	Steel tube	Concrete						
SCW1-1	34.1	65.9	58.8	41.2	62.9	37.1	71.9	28.1
SCW1-2	34.2	65.8	57.6	42.4	62.5	37.5	70.6	29.4
SCW2-1	40.2	59.8	52.7	47.3	55.1	44.9	59.1	40.9
SCW2-2	40.2	59.8	52.6	47.4	54.7	45.3	59.0	41.0
SCW3-1	45.9	54.1	52.6	47.4	54.5	45.5	58.3	41.7
SCW3-2	49.1	50.9	56.5	43.5	55.1	44.9	56.5	43.5

The fracture energy of tensile concrete was used to describe the failure of concrete under tension, which is defined as follows [21]:

$$G_f = a \cdot \left(\frac{f'_c}{10}\right)^{0.7} \times 10^{-3} \cdot (\text{MPa}) \tag{3}$$

where  $G_f$  is fracture energy; coefficient  $a = 1.25d_{max} + 10$ ,  $d_{max}$  is the maximum particle diameter of coarse aggregate.

The elastic modulus of the concrete could be calculated by  $E_c = 3320(f'_c)^{1/2} + 6900$  (MPa), and the Poisson's ratio was 0.2.

3.2. Model building

The three-dimensional eight-node solid element (C3D8R) was used to simulate concrete, steel tube and end plate. The mechanical

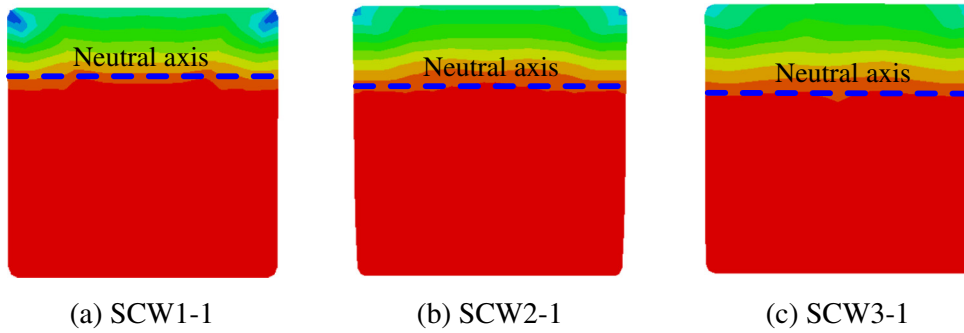


Fig. 15. The location of neutral axis.

parameter of the end plates can hardly affect the behavior of the mid-span section. Therefore, the Young's modulus and Poisson's ratio were defined as  $10^{12}$  MPa and 0.001 separately.

Between the core concrete and steel tube, the surface-to-surface contact was used to simulate the interaction between the two parts, considering the friction in tangent direction. The friction coefficient was defined as 0.6 [20]. Because the stiffness of steel is greater than concrete, the inner surface of the steel tube was defined as the main surface. Between the end plates and the steel tube, the hard contact was used in normal direction only for passing pressure. The same hard contact was used between the end plates and concrete.

The loading was controlled by the vertical displacement, as shown in Fig. 9. To be consistent with the test, one supports was fixed in both Y and Z direction, and the other one was fixed only in Y direction.

### 3.3. Comparison between FEA and test results

The simulation results are compared with the test results as shown in Fig. 10. The simulation results have the same tendency comparing with the test results. To be consistent with the test, the ultimate bearing capacity of the simulation results was also selected when the tensile strain at mid-span reaches  $1000 \mu\epsilon$ . And the differences between the test bearing capacity and the simulated one are limited within 8%, as listed in Table 2.

To demonstrate the stress distribution on the specimen, a corresponding FEA model of test SCW2-2 is given in Fig. 11. Vertical loads were applied until the mid-span deflection was identical to the test mid-span deflection.

It can be seen from Fig. 12 that steel tube and concrete above the neutral axis resisted compression. After the plastic deformation occurred, steel tube began to confine the concrete (shown in Fig. 12(b) and (c)), but effect of the confinement distribution was different along the depth of compression. The concrete cracked at tension side of the beam, steel tube resisted the entire tension, the concrete was not confined. The mechanical performance of HCFHST is similar to the CFST.

Table 5  
Specimens parameters and ultimate bending moment.

Type	Specimen	$t$ (mm)	$f_y$ (MPa)	$f_{cu}$ (MPa)	$M_{ue}$ (kN·m)
Test	SCW1-1	4	434.56	98	70.1
	SCW1-2	4	430	98	65.9
	SCW2-1	5	420	98	90.3
	SCW2-2	5	416.3	98	82.4
	SCW3-1	6	430	98	99.7
	SCW3-2	6	436.9	98	106.6
FEA	ACW-1	4	460	60	71.62
	ACW-2	4	460	80	73.40
	ACW-3	4	460	100	74.88
	ACW-4	4	460	120	76.28
	ACW-5	4	550	100	87.29
	ACW-6	4	690	100	105.17

### 3.4. Analysis on the distribution of the stress

Fig. 12 and Table 3 show the S33 stress of the concrete at mid-span section of feature events A, B and D (Fig. 6). At point A, the distribution of the stress is uniform, neutral axis is slightly higher than the section centric axis, and the stress of point  $d_1$  reached the ultimate tensile stress of concrete. At point B, neutral axis raised a little, stress at point  $a_2$  and  $b_2$  increased. In tensile zone, stress decreased due to the concrete quit working. At point D, neutral axis raised obviously, stress in compressive point  $a_3$  was  $-88.96$  MPa, however, stress in point  $b_3$  was  $-109.08$  MPa. In tensile zone, stress of point  $c_3$  and  $d_3$  were 4.70 MPa and 7.25 MPa. During the whole process, concrete cracked and quit work early in tensile zone.

Fig. 13 and Table 3 demonstrate the Mises stress of the steel tube at mid-span section. At point A, maximum Mises stress at both top and bottom are less than the steel yield stress. So the whole steel tube remains elastic, when the bottom concrete crack at point A. At point B, the maximum Mises stress reaches the steel yield stress, and bottom steel tube starts to yield. However, at point B the top compressive steel remains elastic. At point D, the top steel tube starts to yield, and the yielding extends to about half of the beam height.

### 3.5. The proportion of bear the bearing capacity of each components

Fig. 14 and Table 4 demonstrate the contribution of both concrete and steel tube to the bearing capacity during the whole loading process. Before point A, concrete carry most of the bending moment, about 80%–90%, because the concrete area is much larger than the steel tube, besides, the section remains elastic, so the stress difference between concrete and steel is not much. The concrete cracked at point A, and the proportion of the concrete declined to 50.9%–65.9%. With the raising of neutral axis, the area of compressive region decreased, and the proportion of the steel tube increased to 52.6%–58.8% at point B. When reached event D, the proportion of the steel tube raised to 56.5%–71.9%. Fig. 14 and Table 4 show that the proportion of the steel tube decreases with the increase of steel ratio, because the area of compressive region increases with the steel ratio, as shown in Fig. 15.

## 4. Parameters analysis

To further analyze the effects of different design parameters, steel ratio, steel yield strength and concrete compressive strength are taken as the variables. The design parameters and the corresponding results are shown in Table 5 and Fig. 16.

### (1) The effect of steel ratio

Fig. 16(a) demonstrates the load-deflection curves of the specimens with the different steel ratio. To specimens SCW 1-2, 2-2 and 3-1, the thickness of the steel tube are 4, 5 and 6 mm, respectively. According to Table 3, the ultimate bearing capacity of specimens SCW 2-2 and 3-1 are 125% and

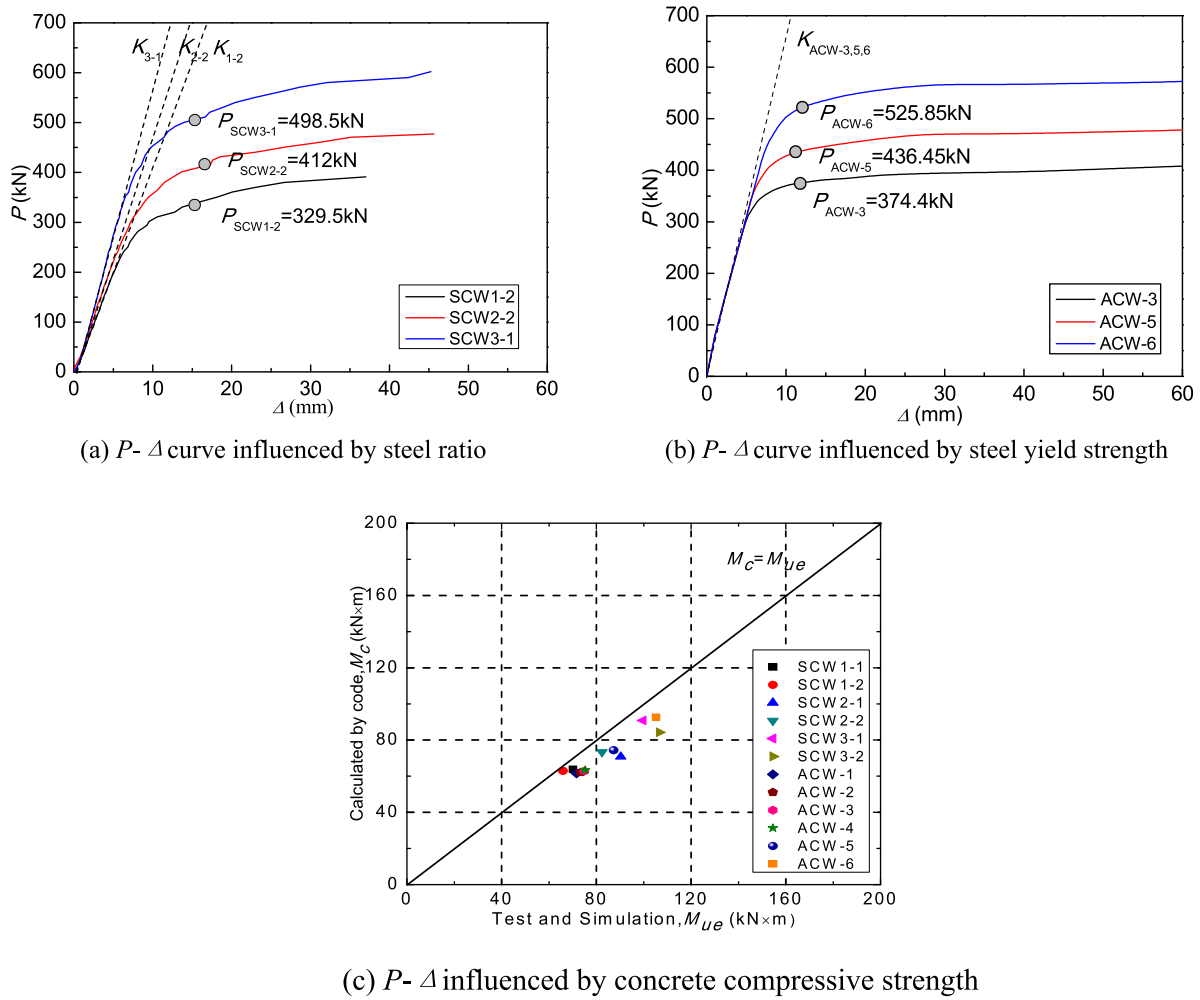


Fig. 16. Comparison of load-deflection curve.

151.3% of the strength of specimen SCW 1-2. This is because that the confinement factor increases  $\xi$  with steel ratio, and the concrete ultimate compressive strength also increases with the confinement factor.

(2) The effect of steel yield strength

Fig. 16(b) demonstrates the load-deflection curves of the specimens with different steel yield strength. To specimens ACW-3, 5 and 6, the steel yield strength are 460 MPa, 550 MPa and 690 MPa, respectively.

According to Table 3, the ultimate bearing capacity of model ACW-5 and 6 are 116.6% and 140.5% of the strength of ACW-3. Besides, the stiffness of the specimens before point B, tensile steel yield, are identical.

(3) The effect of concrete compressive strength

Fig. 16(c) demonstrates the load-deflection curves of the specimens with different concrete compressive strength. To specimens model ACW-1, 2, 3 and 4, the concrete compressive strength are 60, 80, 100

Table 6  
Flexural capacity compared with different codes.

Type	Specimen	$M_{ue}$ (kN·m)	AISC-LRFD (1994)		AII (1997)		EC4 (1994)		GB59036 (2014)	
			$M_c$ (kN·m)	$M_c/M_{ue}$	$M_c$ (kN·m)	$M_c/M_{ue}$	$M_c$ (kN·m)	$M_c/M_{ue}$	$M_c$ (kN·m)	$M_c/M_{ue}$
Test	SCW1-1	70.1	63.85	0.91	63.85	0.91	63.81	0.91	76.17	1.09
	SCW1-2	65.9	62.30	0.95	62.30	0.95	63.18	0.96	75.61	1.15
	SCW2-1	90.3	70.83	0.78	70.83	0.78	74.90	0.83	85.50	0.95
	SCW2-2	82.4	72.67	0.88	72.67	0.88	74.25	0.91	84.99	1.03
	SCW3-1	99.7	88.95	0.89	88.95	0.89	89.29	0.90	96.56	0.97
	SCW3-2	106.6	84.23	0.80	84.23	0.80	90.63	0.85	97.55	0.92
Simulation	ACW-1	71.6	61.53	0.86	61.53	0.86	64.82	0.91	68.14	0.95
	ACW-2	73.4	62.16	0.85	62.16	0.85	66.14	0.90	73.63	1.00
	ACW-3	74.9	62.85	0.84	62.85	0.84	67.28	0.90	79.23	1.06
	ACW-4	76.3	63.35	0.83	63.35	0.83	68.21	0.90	84.58	1.11
	ACW-5	87.3	74.32	0.85	74.32	0.85	79.47	0.91	90.03	1.03
	ACW-6	105.2	92.60	0.88	92.60	0.88	98.21	0.93	106.78	1.02
Mean value ( $\mu$ )				0.86		0.86		0.90		1.02
Standard deviation ( $\sigma$ )				0.04		0.04		0.03		0.02

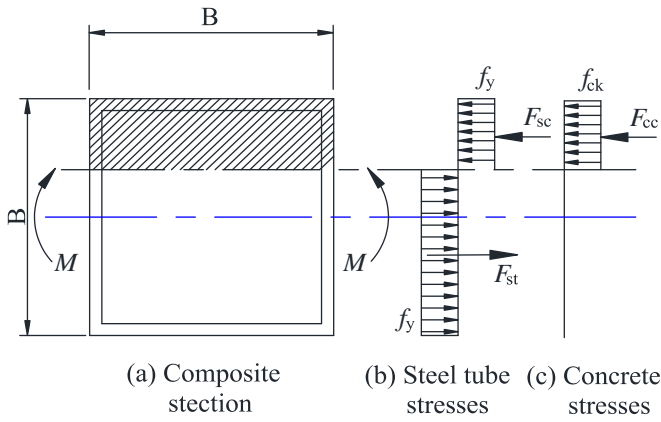


Fig. 17. Diagram for calculation of flexural moment capacity of CFST beam.

and 120 MPa, respectively. According to Table 3, the ultimate bearing capacity of model ACW-2, 3 and 4 are 102.5%, 104.6% and 106.5% of the strength of ACW-1. Besides, the initial stiffness and yield strength are really close to all four models.

### 5. Comparison between different codes

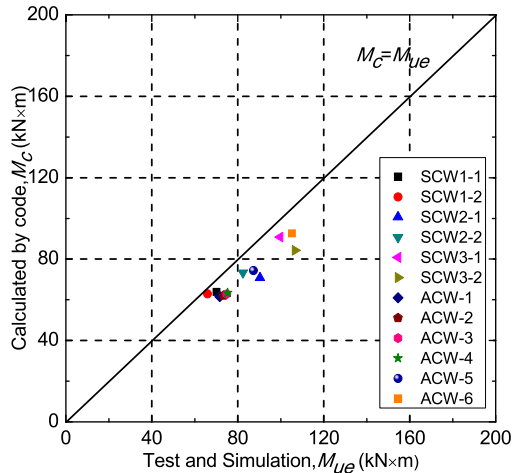
To compare and analyze the current code design methods, the bearing capacity of all the test specimens and simulated models according to the four different codes (AISC-LRFD (1999), AIJ (1997), EC4 (1994) and GB50936-2014(2014)) are listed in Table 6. The methods to calculate the bearing capacity can be separated into 3 types as follows:

- (1) AISC-LRFD (1999) [22] and AIJ (1997) [23] only considered the contribution of the steel tube to the bearing capacity and ignored the effect of concrete. The formulation to calculate bearing capacity is showed as follow:

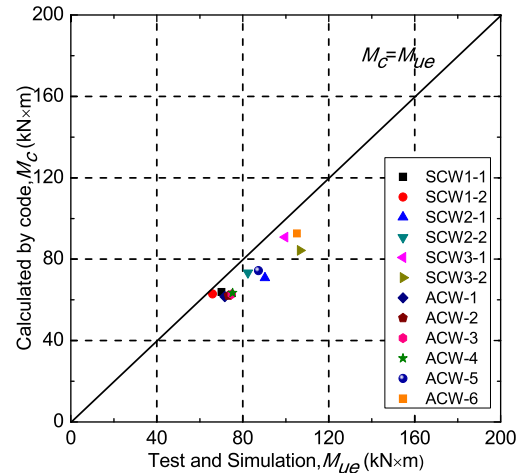
$$M_u = Zf_y \tag{4}$$

where,  $M_u$  is the ultimate bending moment,  $f_y$  is the yield strength of steel,  $Z$  is the plastic section modulus of steel tube,  $Z = B^3t/2 - 2Bt^2 + 2t^3$ ,  $B$  and  $t$  are the width and thickness of the square steel tube, respectively.

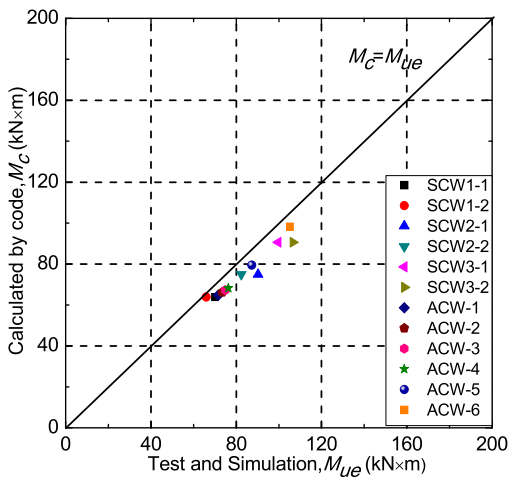
- (2) EC4 (1994) [24] uses the formulation below to calculate bearing capacity:



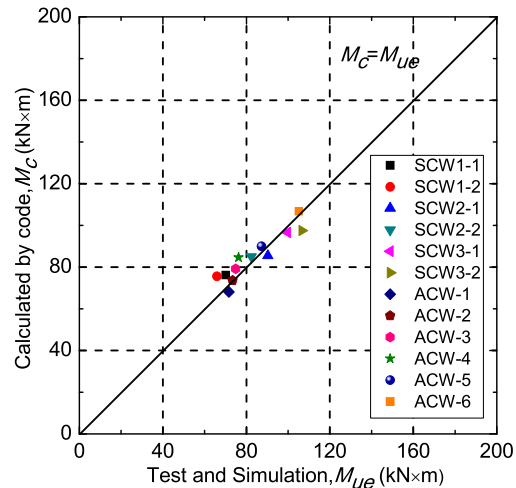
(a) LRFD (1994)



(b) AIJ (1997)



(c) EC4 (1994)



(d) GB50936 (2014)

Fig. 18. Comparison of the flexural bearing capacity.

$$M_u = f_y [(A_s(B-2t-d_c)/2 + Bt(t+d_c))] \quad (5)$$

where,  $d_c = (A_s - 2Bt)/((b - 2t)\rho + 4t)$ ,  $\rho = 0.6f_{ck}/f_y$ ;  $B$  and  $t$  are the width and thickness of the square steel tube, respectively;  $A_s$  is the area of steel tube,  $f_{ck}$  is the characteristic concrete strength. Fig. 17 shows the diagram for calculation the moment capacity of circular CFST beam in EC4.

- (3) GB50936-2014(2014) [25] uses the formulation below to calculate bearing capacity:

$$M_u = \gamma_m W_{sc} f_{sc} \quad (6)$$

where,  $\gamma_m$  is flexural strength index,  $\gamma_m = -0.438\xi + 1.926\sqrt{\xi}$ ,  $\xi = -f_y A_s / f_{ck} A_c$ ;  $W_{sc}$  is the section modulus of the composite section, which can be calculated by  $B^3/6$ ;  $f_{sc}$  is the nominal yield strength of the composite section,  $f_{sc} = (1.212 + B\xi + C\xi^2)$ ,  $B = 0.131f_y/215 + 0.723$ ,  $C = -0.070f_{ck}/14.4 + 0.026$ .

Table 6 shows the results of test values ( $M_{ue}$ ) and calculation values ( $M_c$ ) of the different codes.

As shown in Table 6 and Fig. 18, calculation value of LFRD (1999), AIJ (1997), EC4 (1994) and GB50936 (2014) all matched the test and simulation results, while GB50936-2014 (2014) ( $\mu = 1.02$ ,  $\sigma = 0.02$ ) was the best, but the results was not safety. The calculation results of GB50936 (2014) ( $\mu = 1.02$ ,  $\sigma = 0.02$ ) were little higher than the results calculated by the other three codes, because the LFRD (1999) ( $\mu = 0.86$ ,  $\sigma = 0.04$ ) and AIJ (1997) ( $\mu = 0.86$ ,  $\sigma = 0.04$ ) only considered the contribution of the steel tube for the bearing capacity and EC4 (1994) ( $\mu = 0.90$ ,  $\sigma = 0.03$ ) did not consider the combination effect between steel tube and concrete. Therefore, it can be concluded that EC4 (1994) was the most compatible code to calculate bearing capacity of HCFHST.

## 6. Conclusions

Based on the analysis and discussion on the test and FEA results, the following conclusions can be drawn:

- (1) The HCFHST specimen under pure bending load has a high ductility. The deflection curve performs close to sinusoid shape, and it fails because of the local bulking of the top surface of the steel tube at mid-span.
- (2) The moment–curvature relationship of the HCFHST specimen under pure bending load can be separated into four stages according to the mechanical behavior of the components: elastic stage, yield stage and hardening stage.
- (3) Before concrete crack, core concrete mainly resists the bending moment. After that the proportion of steel tube increases, and after tensile steel yields, steel tube mainly resists the bending moment.
- (4) The ultimate bearing capacity of the HCFHST under pure bending moment significant increases with steel ratio and steel yield strength. The increase due to the core concrete compressive strength is much less than the other two design variables.
- (5) The test and FEA results are more consistent with the design results according to code EC4 (1994) than the results of other three codes. LFRD (1999), AIJ (1997) and EC4 (1994).

## Acknowledgements

This project was supported by National Natural Science Foundation of China (51378319), Innovative Research Team of Higher Education in Liaoning Province (LT2014012), Shenyang Engineering and Technological Research Center for Civil Steel Construction Industrialization (F16-076-8-00).

## References

- [1] A.H. Varma, J.M. Ricles, R. Sause, L.W. Lu, Seismic behavior and modeling of high-strength composite concrete-filled tube (CFT) beam-columns, *J. Constr. Steel Res.* 58 (5) (2002) 725–758.
- [2] A.H. Varma, J.M. Ricles, R. Sause, L.W. Lu, Experimental behavior of high strength square concrete-filled steel tube beam-columns, *J. Struct. Eng.* 128 (3) (2002) 309–318.
- [3] D. Liu, W.M. Gho, J. Yuan, Ultimate capacity of high-strength rectangular concrete-filled steel hollow section stub columns, *J. Constr. Steel Res.* 59 (12) (2003) 1499–1515.
- [4] W.M. Gho, D. Liu, Flexural behavior of high-strength rectangular concrete-filled steel hollow sections, *J. Constr. Steel Res.* 60 (11) (2004) 1681–1696.
- [5] D. Liu, W.M. Gho, Axial load behavior of high-strength rectangular concrete-filled steel tubular stub columns, *Thin-Walled Struct.* 43 (8) (2005) 1131–1142.
- [6] B. Young, E. Ellobody, Experimental investigation of concrete-filled cold-formed high strength stainless steel tube columns, *J. Constr. Steel Res.* 62 (5) (2006) 484–492.
- [7] M. Muris, B. Uy, Behavior and design of fabricated high strength steel columns subjected to biaxial bending part1: experiments, *Adv. Steel Constr.* 2 (4) (2006) 286–313.
- [8] M. Muris, B. Uy, Behavior and design of fabricated high strength steel columns subjected to biaxial bending part 2: analysis and design codes, *Adv. Steel Constr.* 2 (4) (2006) 314–354.
- [9] Y.H. Choi, K.S. Kim, S.M. Choi, Simplified P–M interaction curve for square steel tube filled with high-strength concrete, *Thin-Walled Struct.* 46 (5) (2008) 506–515.
- [10] K.S. Chung, J.H. Kim, J.H. Yoo, Prediction of hysteretic behavior of high-strength square concrete-filled steel tubular columns subjected to eccentric loading, *Int. J. Steel Struct.* 12 (2) (2012) 243–252.
- [11] H.S. Jung, J.H. Chung, C.S. Choi, The behavior of high-strength square steel tube columns filled with concrete, *Adv. Sci. Lett.* 13 (1) (2012) 146–151.
- [12] K.S. Chung, J.H. Kim, J.H. Yoo, Experimental and analytical investigation of high-strength concrete-filled steel tube square columns subjected to flexural loading, *Steel Compos. Struct.* 14 (2) (2013) 133–153.
- [13] S. Guler, A. Copur, M.A. Aydogan, Comparative study on square and circular high strength concrete-filled steel tube columns, *Adv. Steel Constr.* 10 (2) (2014) 234–247.
- [14] G.C. Li, Y. Liu, B.W. Zhu, High-strength concrete filled high-strength steel tube finite element analysis of stub column under axial compressive load, 7th European Conference on Steel and Composite Structures, Napoli, Italy, 2014.
- [15] V.I. Patel, Q.Q. Liang, M.N.S. Hadi, Numerical analysis of high-strength concrete-filled steel tubular slender beam-columns under cyclic loading, *J. Constr. Steel Res.* 92 (2014) 183–194.
- [16] C.S. Kim, H.G. Park, K.S. Chung, I.R. Choi, Eccentric axial load capacity of high-strength steel-concrete composite columns of various sectional shapes, *J. Struct. Eng.* 140 (4) (2013) 04013091.
- [17] S.T. Zhong, The unified theory of concrete filled steel tube (CFST), *Harbin Archit. Civ. Eng. Inst.* 12 (6) (1994) 21–27.
- [18] L.H. Han, *Concrete Filled Tubular Structures—theory and Practice*, Science Press, Beijing, 2004.
- [19] L.H. Han, G.H. Yao, Z. Tao, Performance of concrete-filled thin-walled steel tubes under pure torsion, *Thin-Walled Struct.* 45 (1) (2007) 24–36.
- [20] FIP, CEB-FIP Model Code 1990, Thomas Telford Ltd., London, 1993.
- [21] AISC, Load and Resistance Factor Design Specification for Structural Steel Buildings, American Institute of Steel Construction Inc., Chicago, 1999.
- [22] Architectural Institute of Japan (AIJ), Recommendations for Design and Construction of Concrete Filled Steel Tubular Structures, October, 1997.
- [23] Eurocode 4 (EC4), Design of Composite Steel and Concrete Structures—Part-1: General Rules and Rules for Building, CEN, Brussels, 2004.
- [24] GB50936-2014, Technical Code for Concrete Filled Steel Tubular Structures, Ministry of Housing and Urban-Rural Development of the People's Republic of China, China Architecture & Building Press, Beijing, 2014.